

Biophysical Journal, Volume 117

Supplemental Information

**The Interplay Between Cell-Cell and Cell-Matrix Forces Regulates Cell
Migration Dynamics**

Apratim Bajpai, Jie Tong, Weiyi Qian, Yansong Peng, and Weiqiang Chen

Supporting Methods

1. Thin-sheet FEM model and Intercellular force calculation

Previous studies have employed several methods to measure intercellular forces using mechanical imbalance of traction forces between two cells or multiple cells⁽¹⁻³⁾. We adopted a finite element method (FEM) model in this study, based on thin plate model of linearly elastic and isotropic substances. We used patterned cell layers devoid of any gaps among cells, to ensure that patterned cells form a flat, thin sheet, where the height is infinitesimally small compared to the diameter of the patterned cell monolayer. Traction forces were calculated using traction force microscopy (**Fig. S1a**) and only the in-plane components of traction forces were considered in this model. Newton's laws dictate that internal stresses must be balanced by traction forces⁽⁴⁾, resulting in a relationship between the recovered traction forces and sheet stresses. According to the model, the stresses in the plate are related to the strains by the Equation 1.1:

$$\begin{bmatrix} \sigma_{xx} \\ \sigma_{yy} \\ \sigma_{xy} \end{bmatrix} = \frac{E}{1 - \nu^2} * \begin{bmatrix} 1 & \nu & 0 \\ \nu & 1 & 0 \\ 0 & 0 & \frac{1 + \nu}{2} \end{bmatrix} \quad (\text{Equation 1.1})$$

where, E is the Young's modulus of the elastic material, and ν is the Poisson's ratio. In our model, $E = 16.2$ kPa and $\nu = 0.5$, as cells are incompressible in the scenario considered.

Further, the strains are related to the displacement by the Equation 1.2:

$$\begin{bmatrix} \epsilon_{xx} \\ \epsilon_{yy} \\ \epsilon_{xy} \end{bmatrix} = \begin{bmatrix} \frac{du_x}{dx} \\ \frac{du_y}{dy} \\ \frac{1}{2} * \left(\frac{du_x}{dy} + \frac{du_y}{dx} \right) \end{bmatrix} \quad (\text{Equation 1.2})$$

The traction force in the sheet are related to the stress by the Equation 1.3:

$$\frac{d\sigma_{ij}}{dj} = -h * T_j, \text{ over the entire region of interest} \quad (\text{Equation 1.3})$$

where, T_j is the traction component in the j direction measured by traction force microscopy (TFM) (**Fig. S1b**).

This gives us a set of elliptical boundary value problems that can be solved with FEM. In this case, we modified a MATLAB code⁽³⁾ that was used to solve the partial differential equations (PDEs) to calculate for sheet stresses acting inside the cellular colony, and subsequently intercellular forces in a cellular colony. For cells seeded on a circular pattern, the mask covering all the cells attached to the substrate in the pattern was taken as the geometry.

The MATLAB program solved the elliptical PDE's under free boundary conditions. After determining the stresses acting inside the colony, the intercellular forces between two cells was calculated by the Equation 1.4:

$$f_{1,2} = - \int \sigma \cdot dl , \text{ over the boundary, } 1 \rightarrow 2 \quad (\text{Equation 1.4})$$

The vector, dl is a vector that is perpendicular to the cell boundary and pointing towards the inside of the cell (**Fig. S1c**). The intercellular forces are in the form of a vector acting at different points along the cellular periphery. Previous studies have reported that, in confluent patterns, a majority of microtubule organization centers are approximately found at the cell nucleus⁽⁵⁾. Hence, we calculated the torque of the forces along the cell nucleus to gauge the twisting capabilities of the intercellular force acting on a single cell. Torque of a single cell's force is given by the equation:

$$T = \sum \vec{r} \times f_1 , \text{ over the boundary or cell} \quad (\text{Equation 1.5})$$

where, \vec{r} is the vector from the cell nucleus to the force's point of action, and f_1 is the intercellular force acting at a point on the cell's periphery.

2. Analysis on the impact of boundary selection with phase-field vs. fluorescent images

We used phase-field images for boundary selection in this study. In order to prove the robustness of our approach, we used human vein endothelial cells (hUVEC) (**Fig S2c, d**) live stained with FITC anti-human CD31 antibody (**Fig. S2b, d**). We independently selected cellular boundary using phase-field and fluorescence images. We observed very small differences in the interface selection between the two approaches, as shown in **Fig. S2e, f**, where the ratio of intersectional area between cells selected from phase-field and cell staining images, divided by average cellular area of cells selected from phase-field and cell staining images came out to around ~ 0.86 , whereas a difference of $\sim 1.48 \mu\text{m}$ was observed between the boundaries selected by phase-field and cell staining images. Further, we calculated the cell traction forces and intercellular forces in the cell monolayer and, found a very strong correlation between the traction force and intercellular forces calculated using the boundaries selected through the phase-field images and the staining images (**Fig S2g, h**).

3. Effect of cell density on cell forces in micropatterns

In order to understand the effect of density on the cellular monolayers, we cultured cellular monolayers with different seeding density (**Fig. S3**) to acquire, sub-confluent, low-density confluent and high-density confluent cellular patterns as shown in **Fig. S3a**. We also cultured an over-confluent confined cellular assembly by seeding a cellular monolayer of cells and letting it grow for 48 hours. Our study showed that the seeding density drastically effects various morphological and dynamic properties of the cells in these confined patterns.

The first immediately visible change was observed in cellular velocity, which decreased significantly with an increase in seeding cellular density which may be a result of increased intercellular friction⁽⁶⁻⁸⁾. We introduced order parameter, defined by **Equation 1.6**:

$$\text{Order parameter} = \frac{\text{Perimeter}}{\sqrt{\text{Area}}} \quad (\text{Equation 1.6})$$

The order parameter of the cell has been shown in previous studies to be correlated with the phase transition in confined cellular monolayers and it has been shown that the phase transition occurs around order parameter equal to 3.813⁽⁸⁻¹⁰⁾. We found that the order parameter decreased

with the seeding cell density (**Fig S3e**). In confluent patterns, we see that with increasing density the cellular morphology regularizes and more closely resembles an immobile solid like state, as indicated by the decreasing cellular velocity (**Fig S3d**).

Further, we explored the effect of density on the forces exerted by the cells. We found that the force exerted by the cells first increases with increasing seeding density, and transitions from sub-confluent to confluent patterns (**Fig S3b, f**). However, once confluence is reached further increase in initial seeding density of the cells, leading to a higher density confluent patterns does not result in higher forces but rather a concentration of forces at the cellular periphery and a decrease in overall forces (**Fig S3b, f**). Further, we found that the magnitude of intercellular forces exerted by cells in high density patterns to be lower than the low-density patterns (**Fig S3g**). This is in accordance with the results displayed in previous studies which have shown that the intercellular forces are proportional to the magnitude of the traction forces exerted by the cells⁽¹¹⁾. However, the more interesting result is the correlation of cellular density with the ratio of cell adhesive traction and intercellular force, where we observed that the low-density patterns have a significantly higher ratio of cell traction to intercellular force as compared to high density patterns (**Fig S3h**). This is in accordance with the previously published results that show that the transition from liquid to solid phase is associated with an increase in the cell-cell forces and a decrease in motility⁽¹²⁾.

4. Characteristics of traction and intercellular forces

We manually selected and traced cells in the patterns from phase-field images to create cell regions of interests (ROIs). Once we defined ROIs, traction and intercellular forces acting on the cells were calculated. In accordance with the established results of traction forces exerted by single cells⁽¹³⁾, we determined that cells with larger spreading area apply larger forces (**Fig. S4b**). Furthermore, we showed that traction forces vary with the order parameter (**Fig. S4c**) of a cell.

Traditionally, single cells that demonstrate higher order parameter are known to exhibit higher traction forces. We found a similar trend in the cells inside a confluent colony. The other significant force in the patterned cell monolayer is the intercellular force. We demonstrated that there are two types of intercellular force, normal forces (**Fig. S4a (i,ii)**), and tangential forces (**Fig. S4a (iii)**), which may imply that the cells not only push and pull on each other but may also apply shear forces capable of twisting effects. We determined that the total intercellular force acting on a single cell is dependent upon two critical factors: the number of neighboring cells (**Fig. S4d**) and the length of a cell-cell interface (**Fig. S4e**). For both cases, it was found that the cells have a positive correlation with the critical factors.

5. Correlation of nuclear translation with cell centroid and centrosome translations

In our study, we used the cellular nucleus as the reference for determining cellular migration. Here, we showed a correlation between the cellular nuclear centroid and the cellular centroid that is traditionally used in studies on cellular migration. **Fig. S5a** shows the nuclear centroid and cellular trajectory of a single cell migrating over a period of 240 minutes, which shows a strong correlation between the cellular nucleus and the cellular centroid position. Not only this, we observed a very strong correlation between the cell centroid displacement and the nuclear displacement as shown by the scatter graph in **Fig. S5c**. Having established the validity of using

cellular nucleus in isolated single cells, we next showed the same association in cells inside a confluent monolayer.

Order parameter (Eq. 1.6) is associated with the polarity of cellular morphology^(8, 9). Cellular elongation has been linked with cellular migration^(14, 15). However, it is not the defining factor with regards to cellular migration. In order to prove this, we followed 4 cells, two elongated and two rounded as they migrated over a period of 240 minutes. **Fig. S5d** shows the phase-field image of four cells in a confluent micropattern, and **Fig. S5e** shows an overlapped nuclear and cell centroid trajectory for the cells, which reiterates the correlation that we observed in isolated single cells. Further, we measured the order parameter of the cells as they migrated, and we found that the cells do not show significant changes in their morphological states (**Fig. S5g**). Finally, **Fig. S5g, h, i** show the nuclear and cellular centroid trajectory of one of cells used in the translational analysis in the study. We observed a very strong correlation between the cell centroid displacement with the nuclear centroid displacement for all the 10 cells used in translation analysis.

Further, we transfected C166 cells with pEGFP-ninein C-ter (Addgene plasmid #73523B), to visualize cellular centrosomes and correlate nuclear migration with cell centrosome migration. We found that in translating cells, the cellular centrosome and nucleus moved in tandem as shown in **Fig. S6c, d**. We quantified the translational results over a period of 45 minutes and found that there is a very strong correlation between centrosome translation and nuclear translation (**Fig 6e, f**), further validating our use of nuclear centers as the determinant of cellular migration.

6. Correlation of nuclear rotation with cellular orientation

We correlated the strong association of nuclear orientation with cellular orientation. We observed 4 types of cells inside the confluent monolayer, based on their morphology and the migration behavior, elongated cells, elongated with a very high order parameter associated with them; non-elongated migrating cells, rounded with significant translation; non-elongated stationary cells, rounded and stationary; and lastly dividing cells that underwent division during the observation window. Elongated and non-elongated cells were distinguished using the order parameter (**Fig. S7c**). Phase-field image of the cells is shown in **Figure S7a**. We used three factors to correlate the cellular nuclear orientation with cellular orientation (**Fig. S7b**). Elongated cells offer an evident cellular axis and we used the angular difference between the nuclear orientation and the cellular orientation as a measure of correlation. Non-elongated translating cells do not offer any such principle cellular orientation; hence we used the difference between the cellular migration direction and the nuclear orientation as a measure of correlation. Along with this we also used the angular velocity of the nucleus as the measure of the nuclear reorientation.

The angular velocity measurements showed that dividing cells had a significantly larger angular velocity as compared to the other cells. Similarly, non-translating cells had a significantly higher nuclear angular velocity as compared to the translating and the elongated cells (**Fig. S7d**). We showed that there was a very small angular difference between the cellular orientation and nuclear orientation in elongated cells and similarly a slightly higher but still small angular difference between the nuclear orientation and the cell migration direction in case of translating

cells. We followed an elongated cell and two translating cells, as an example to show the correlation between the nuclear orientation and the cellular orientation in these cells.

Hence, we confirmed that irrespective of the cellular morphology, translating cells have a very high correlation with the nuclear orientation. This correlation increases with increasing elongation of the cells. In terms of the nuclear reorientation, three distinct states exist in the monolayers; a rigid state during migration, a plastic stage while the cells are stationary and a hyper excited stage prior to migration.

Supporting Figures

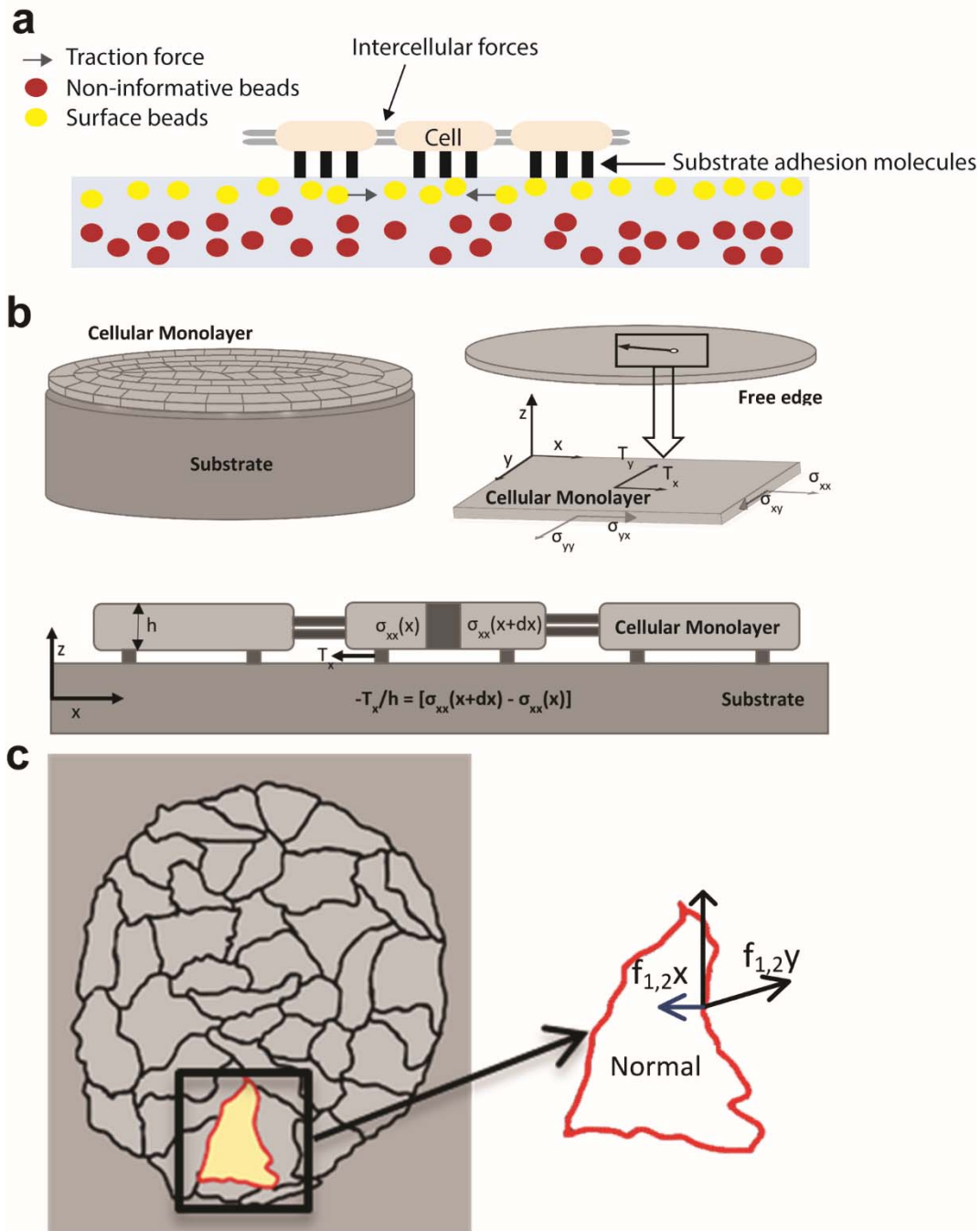


Figure S1. TFM measurement and thin-sheet FEM model for calculating intercellular forces. (a) Schematic of measuring traction forces using TFM. Diagrams illustrating (b) thin-sheet FEM model for intercellular force calculations (c) using a single cell's contour and the traction stresses.

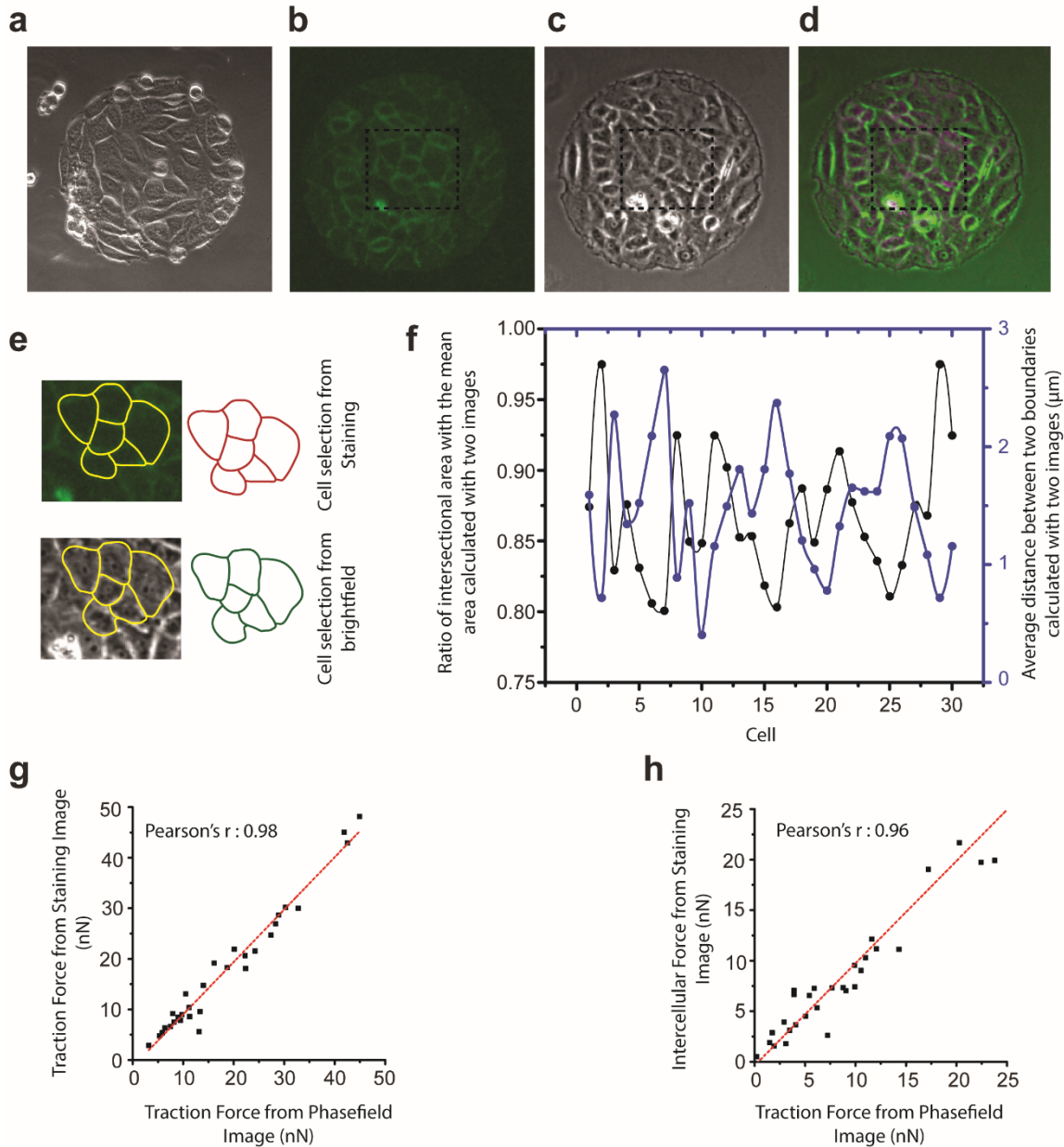


Figure S2. Correlating calculation of forces using staining image and phasefield image. (a) Phasefield image of a C166 colony on a confined micropattern. (b) Staining image showing CD 31 expressed in HUVECs. (c) Phasefield image of HUVECs on a confined micropattern. (d) Merged image showing both staining and phasefield image. (e) Cells selected using staining image and brightfield image of the cells. (f) Ratio of the intersectional area with the mean area calculated with two images and the average distance between two boundaries calculated with two images, for the 30 cells used in the analysis. (g) Correlation of traction forces calculated from phasefield images and CD31 stained images of the cells showing a Pearson's r of 0.98. (h) Correlation of intercellular forces calculated from phasefield images and CD31 stained images of the cells showing a Pearson's r of 0.96. Number of cells = 30, Number of experiments = 3.

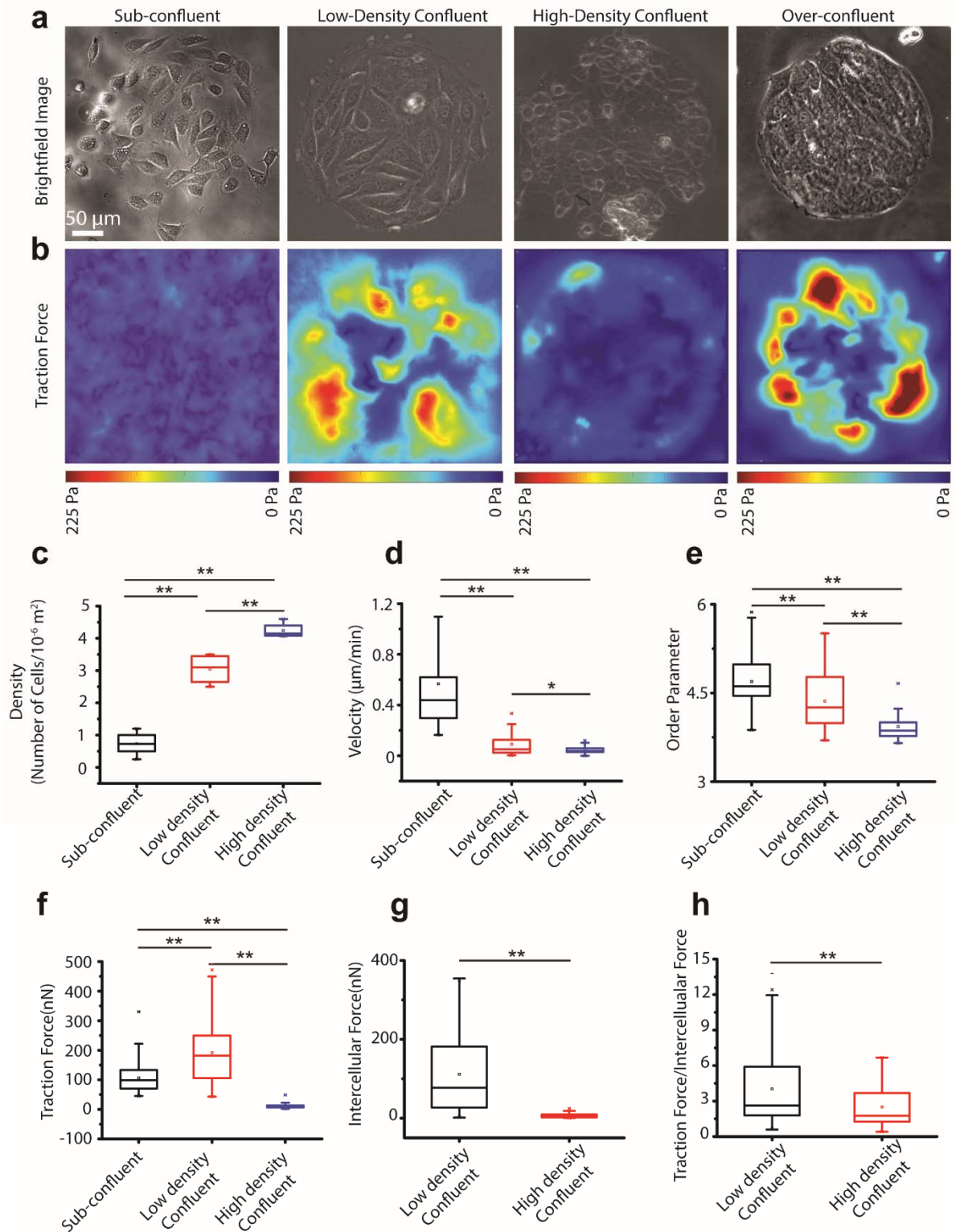


Figure S3. Effect of cellular density on cells in confined micropatterns. (a) Phase-field image of cells with increasing cellular density in confined micropatterns. (b) Corresponding traction force distributions in the micropatterns. (c) Bar graph showing the quantification of cellular density in sub-confluent, low density confluent and confluent micropatterns. (d) Bar graph

showing the quantification of cellular velocities in micropatterns of different densities. (e) Bar graph showing the order parameter of cells in micropatterns of different densities. (f) Bar graph of the traction forces exerted by cells in patterns of different densities. (g) Intercellular force exerted by cells in low and high density confluent micropatterns. (h) Ratio of traction force to intercellular force in confluent patterns of low and high cellular density. Data represent the mean \pm error. The p-values were calculated using the Student's paired sample t-test. *p < 0.05, **p < 0.001. Number of patterns = 5, 5, 5 respectively for sub-confluent, low density and high-density confluent patterns respectively, Number of cells = 50 for each cellular density, Number of experiments = 3 for sub-confluent pattern, and high-density confluent pattern, Number of experiments = 4 for low density confluent pattern.

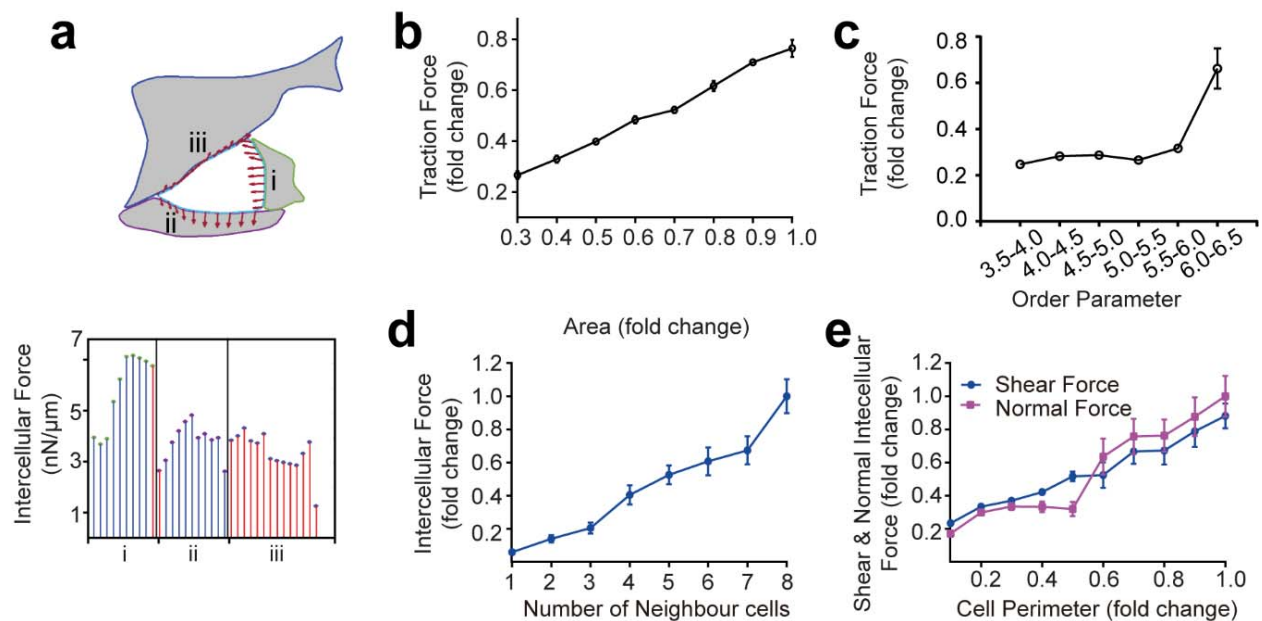


Figure S4. Characteristics of traction and intercellular forces of a single cell. (a) Typical intercellular force distribution around a cell, with three different types of forces, (i) compressive, (ii) extensive and (iii) shear. Variation of traction forces acting on a single cell with respect to the (b) cell area and (c) the cell order parameter. (d) Variation of intercellular forces acting on a single cell with respect to the number of neighboring cells. (e) Variation of shear and normal intercellular force changes with respect to a single cell's perimeter.

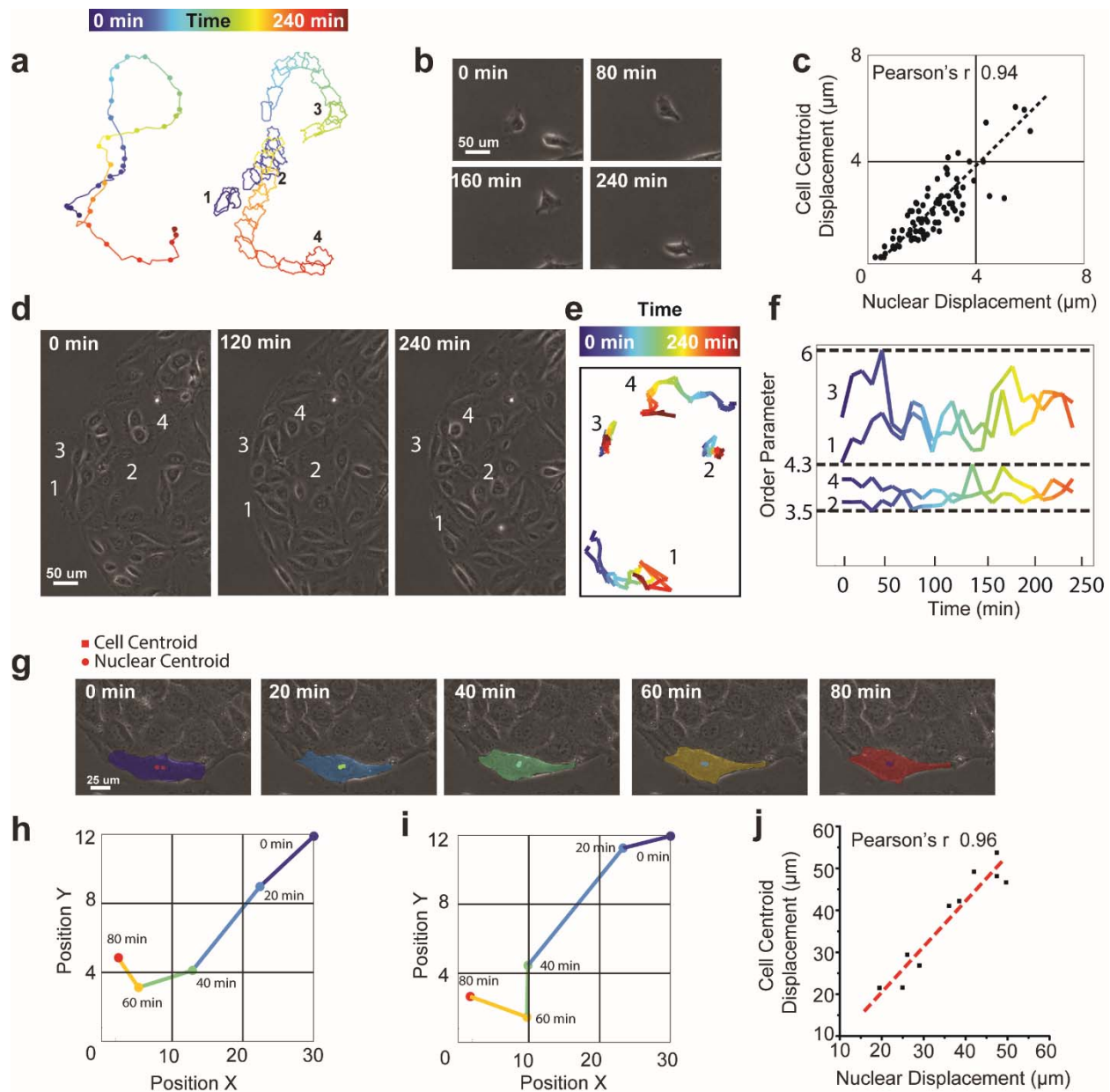


Figure S5. Correlation of nuclear translation with cell centroid translation. (a) Figure showing the nuclear and cellular trajectory of a single cell migrating over a period of 240 minutes. (b) Phase-field image of the cells at the four different points in cellular trajectory. (c) Scatter graph showing the correlation of cell centroid displacement with the nuclear displacement with a Pearson's r of 0.94. (d) Phase-field image of four cells in a confluent micropattern, with two rounded cells and two elongated cells. (e) Plot showing the overlapped nuclear and cell centroid trajectory for the cells over a period of 240 minutes. (f) Plot showing the change in the order parameter of cells over a period of 240 minutes. (g) Figure showing the nuclear centroid and cellular centroid of a cell in a low density confluent micropattern. (h) Plot of the nuclear centroid translation. (i) Plot of the cellular centroid translation. (j) Correlation of the cell centroid displacement with the nuclear centroid displacement for the 10 cells used in translation analysis.

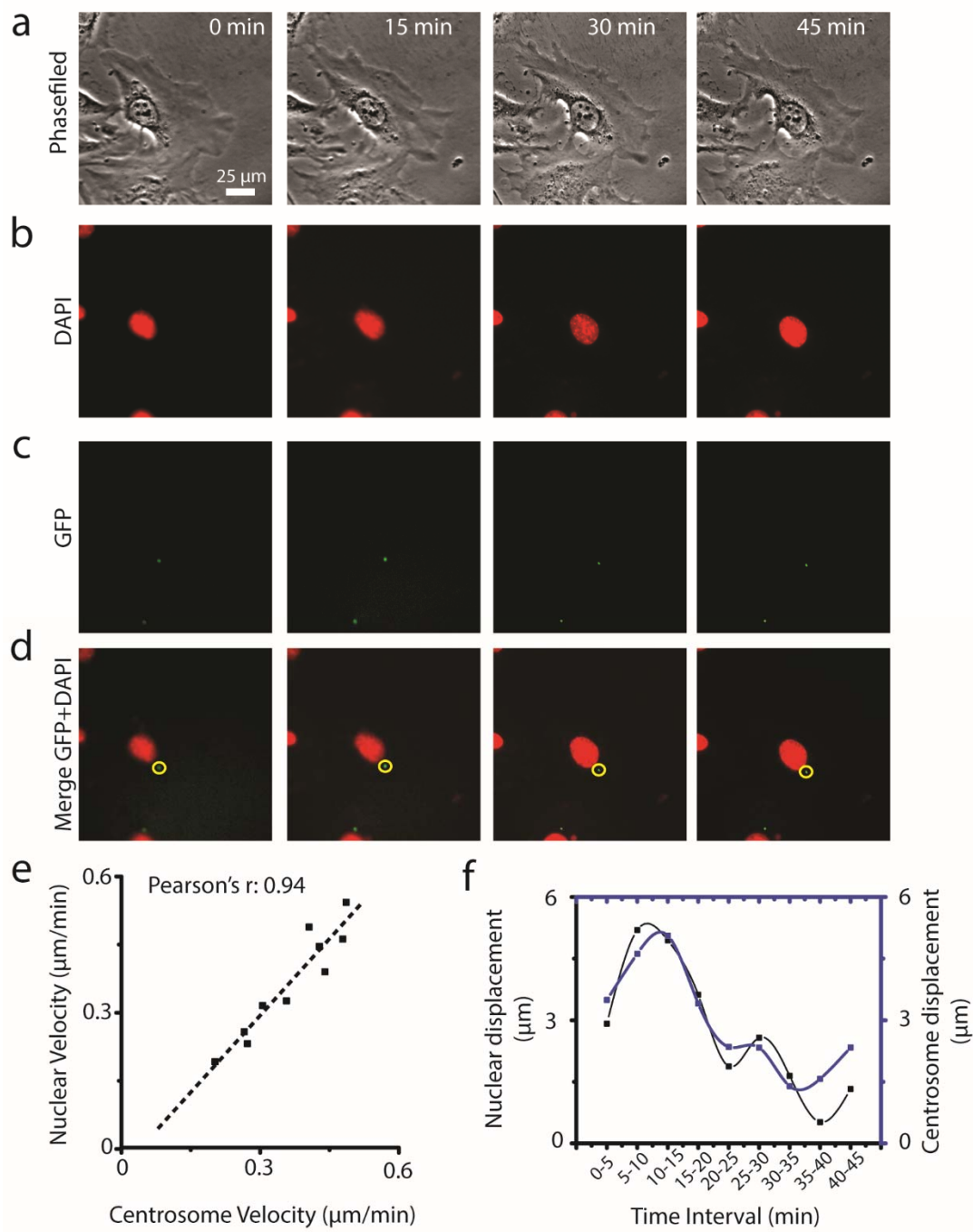
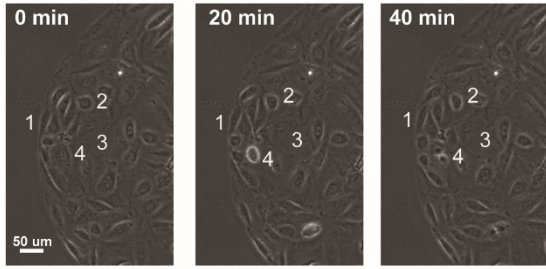


Figure S6. Correlation of nuclear translation with centrosome translation. (a) Phase-field image of translating cells. (b) Fluorescent (DAPI) images of cellular nucleus. (c) Fluorescent (GFP) images of cellular centrosomes. (d) Merged channel image showing both the DAPI and GFP channels. (e) Plot showing the correlation of centrosome and nuclear velocity as the cell translates over a period of 45 minutes. (Number of cells = 12, Number of experiments = 3.) (f) Sample correlation of centrosome displacement with nuclear displacement for the cell shown in a- d.

a

1 Elongated Cells 3 Non-Elongated Stationary Cells
 2 Non-Elongated Translating Cells 4 Dividing Cells

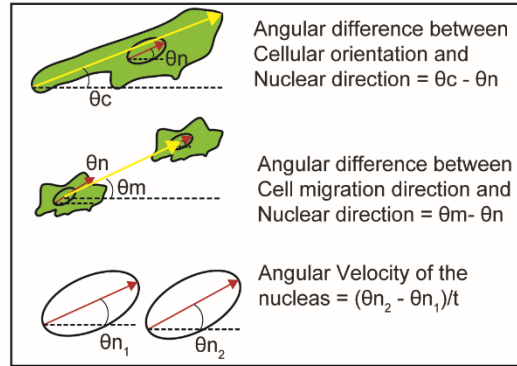
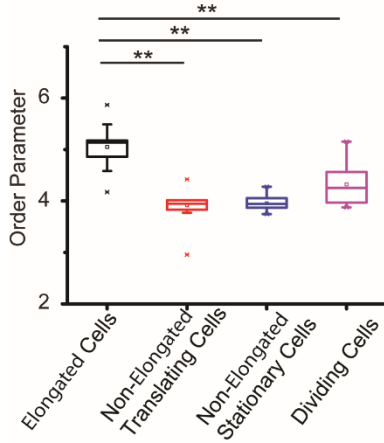
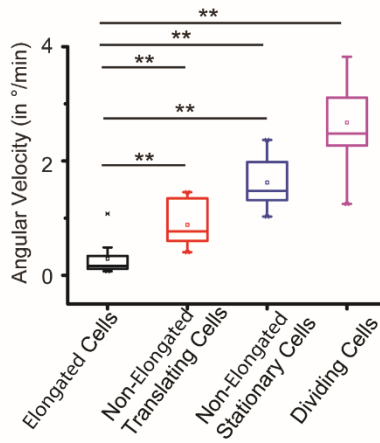
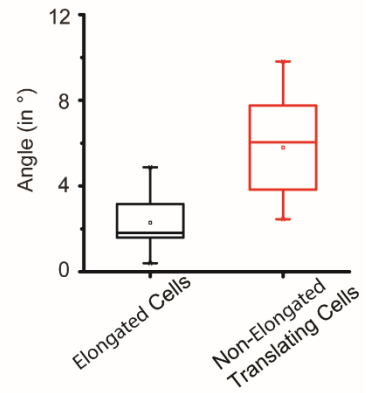
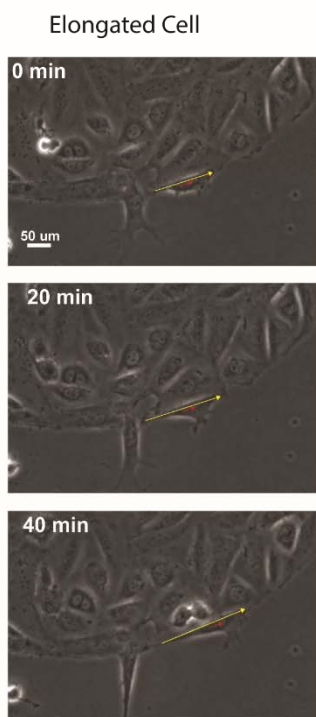
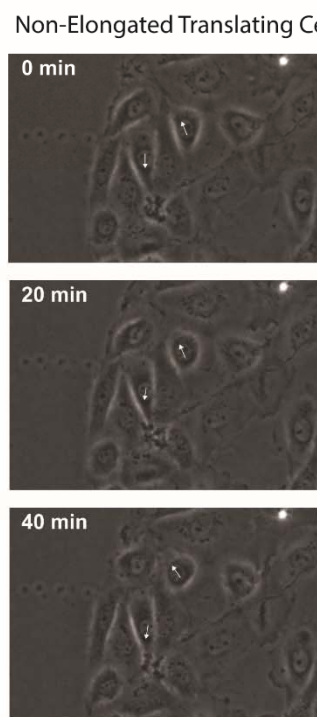
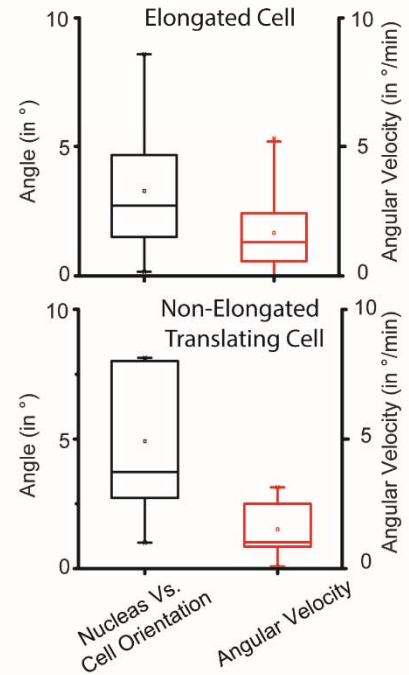
b**c****d****e****f****g****h**

Figure S7. Correlation of nuclear orientation with cellular orientation. (a) Phase-field image of the cells at the four different types of cells in confluent colony, elongated cells, Non-Elongated translating cells, Non-Elongated stationary cells, and dividing cells. (b) Method used to calculate three factors used in correlating nuclear orientation with cellular orientation. (c) Bar graph showing the differences in order parameters of the different types of cells. (d) Bar graph showing the angular velocity as defined in (b), of the different types of cells in the pattern. (e) Angular difference between the cellular orientation and nuclear orientation in case of elongated cells, and the angular difference between the nuclear orientation and the cell migration direction in case of translating cells. (f) Phase-field image showing nuclear orientation of translating cells over a period of 40 minutes. (g) Phase-field image showing cellular orientation and the nuclear orientation of an elongated cell over a period of 40 minutes. (h) Bar graph showing the angular difference between the nuclear orientation and the cellular orientation and the angular velocity of the elongated cell in (f). (i) Bar graph showing the angular difference between the nuclear orientation and the cellular translation direction and the angular velocity of the elongated cells in (g). Data represent the mean \pm error. The p-values were calculated using the Student's paired sample t-test. *p < 0.05, **p < 0.001. Number of cells = 12 for each cell type, Number of experiments = 3.

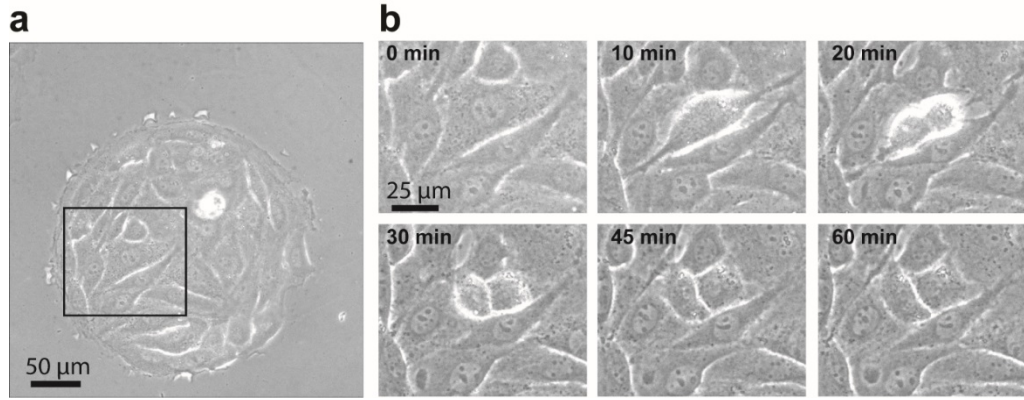


Figure S8. Cell division process. (a) Phase-field image of the pattern at $t=0$ min. (b) Dividing cell at different time points showing the division process and the resulting daughter cells.

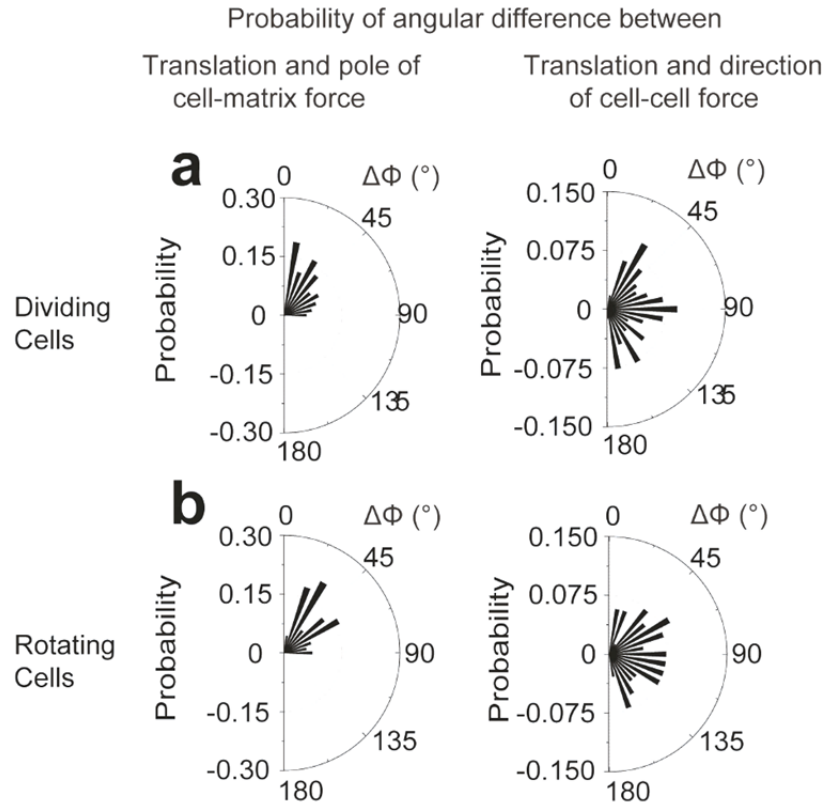


Figure S9. Relationship of translational motion of dividing and stationary cells with the pole of cell-matrix and cell-cell forces. (a) Probability of angular difference between translation direction and the pole of cell-matrix force, and the direction of cell-cell force in case of dividing cells. (b) Probability of angular difference between translational direction and the pole of cell-matrix force, and the direction of cell-cell force in case of rotating cells.

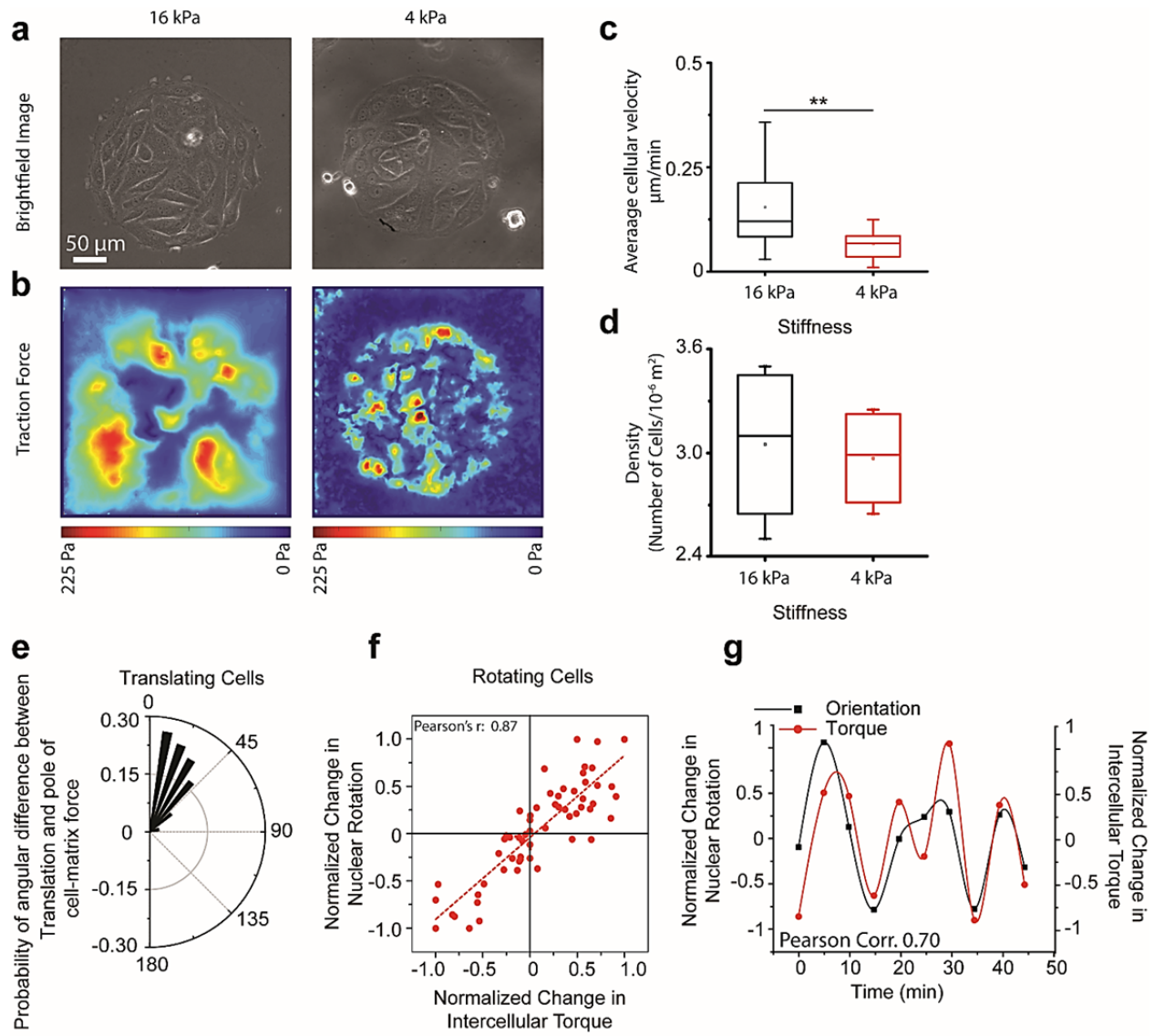


Figure S10. Effect of stiffness on cells in micropatterns. (a) Phase-field image of cells on substrates of different stiffness. (b) Traction stress map of cells on substrates of different stiffness. (c) Average cellular velocity of cells on substrates of different stiffness. (d) Densities of cells on substrates of different stiffness. (e) Probability of angular difference between translation and the pole of cell-matrix force, and the direction of cell-cell force in case of translating cells on 4 kPa substrates. (f) Correlation of normalized change in nuclear rotation with the normalized change in intercellular torque showing a Pearson's r of 0.87 on 4 kPa substrates. (g) Sample correlation curve of normalized change in nuclear rotation and normalized change in Intercellular torque for a single cell with a Pearson's r of 0.70. Data represent the mean \pm error. The p -values were calculated using the Student's paired sample t -test. * $p < 0.05$, ** $p < 0.001$. Number of cells: 6, 6 for translating and rotating cells respectively, Number of experiments = 3.

References

1. Ting, L., J. R Jahn, J. I Jung, B. R Shuman, S. Feghhi, S. Han, M. Rodriguez, and N. Sniadecki. 2012. Flow mechanotransduction regulates traction forces, intercellular forces, and adherens junctions.
2. Liu, Z., J. L. Tan, D. M. Cohen, M. T. Yang, N. J. Sniadecki, S. A. Ruiz, C. M. Nelson, and C. S. Chen. 2010. Mechanical tugging force regulates the size of cell–cell junctions. *Proceedings of the National Academy of Sciences* 107(22):9944.
3. Ng, M. R., A. Besser, J. S. Brugge, and G. Danuser. 2014. Mapping the dynamics of force transduction at cell–cell junctions of epithelial clusters. *eLife* 3:e03282.
4. Tambe, D. T., C. C. Hardin, T. E. Angelini, K. Rajendran, C. Y. Park, X. Serra-Picamal, E. H. Zhou, M. H. Zaman, J. P. Butler, D. A. Weitz, J. J. Fredberg, and X. Trepat. 2011. Collective cell guidance by cooperative intercellular forces. *Nature materials* 10(6):469-475. Research Support, N.I.H., Extramural Research Support, Non-U.S. Gov't.
5. Hale, C. M., W. C. Chen, S. B. Khatau, B. R. Daniels, J. S. Lee, and D. Wirtz. 2011. SMRT analysis of MTOC and nuclear positioning reveals the role of EB1 and LIC1 in single-cell polarization. *Journal of cell science* 124(Pt 24):4267-4285. Research Support, N.I.H., Extramural.
6. Deforet, M., M. C. Parrini, L. Petitjean, M. Biondini, A. Buguin, J. Camonis, and P. Silberzan. 2012. Automated velocity mapping of migrating cell populations (AVeMap). *Nature Methods* 9:1081.
7. Garcia, S., E. Hannezo, J. Elgeti, J.-F. Joanny, P. Silberzan, and N. S. Gov. 2015. Physics of active jamming during collective cellular motion in a monolayer. *Proc Natl Acad Sci U S A* 112(50):15314-15319.
8. Oswald, L., S. Grosser, D. M. Smith, and J. A. Käs. 2017. Jamming transitions in cancer. *Journal of Physics D: Applied Physics* 50(48):483001.
9. Park, J.-A., L. Atia, J. A. Mitchel, J. J. Fredberg, and J. P. Butler. 2016. Collective migration and cell jamming in asthma, cancer and development. *Journal of Cell Science* 129(18):3375.
10. Angelini, T. E., E. Hannezo, X. Trepat, M. Marquez, J. J. Fredberg, and D. A. Weitz. 2011. Glass-like dynamics of collective cell migration. *Proceedings of the National Academy of Sciences* 108(12):4714.
11. Maruthamuthu, V., B. Sabass, U. S. Schwarz, and M. L. Gardel. 2011. Cell-ECM traction force modulates endogenous tension at cell–cell contacts. *Proceedings of the National Academy of Sciences* 108(12):4708.
12. Sadati, M., N. Taheri Qazvini, R. Krishnan, C. Y. Park, and J. J. Fredberg. 2013. Collective migration and cell jamming. *Differentiation* 86(3):121-125.
13. Rape, A. D., W.-H. Guo, and Y.-L. Wang. 2011. The regulation of traction force in relation to cell shape and focal adhesions. *Biomaterials* 32(8):2043-2051.
14. Ridley, A., M. A Schwartz, K. Burridge, R. Firtel, M. H Ginsberg, G. Borisy, J. Thomas Parsons, and A. Rick Horwitz. 2004. *Cell Migration: Integrating Signals from Front to Back*.
15. Kim, D.-H., S. Cho, and D. Wirtz. 2014. Tight Coupling Between Nucleus and Cell Migration through the Perinuclear Actin Cap.